

Efficient Analysis of Geometrical Uncertainty in the FDTD Method using Polynomial Chaos with Application to Microwave Circuits

Andrew C. M. Austin *Member, IEEE* and Costas D. Sarris *Senior Member, IEEE*

Abstract—A novel FDTD-based method is developed to analyze three-dimensional microwave circuits with uncertain parameters, such as variability and tolerances in the physical dimensions and geometry introduced by manufacturing processes. The proposed method incorporates geometrical variation into the FDTD algorithm by appropriately parameterizing and distorting the rectilinear and curvilinear computational lattices. Generalized polynomial chaos is used to expand the time-domain electric and magnetic fields in terms of orthogonal polynomial chaos basis functions of the uncertain mesh parameters. The technique is validated by modelling several microstrip circuits with uncertain physical dimensions and geometry. The computed S -parameters are compared against Monte Carlo simulations, and good agreement for the statistics is observed over 0–25 GHz. A considerable computational advantage over the Monte Carlo method is also achieved.

Index Terms—FDTD, statistical modeling, microwave circuit modeling, stochastic analysis, uncertainty

I. INTRODUCTION

COMPUTATIONAL electromagnetic techniques, such as the Finite-Difference Time-Domain (FDTD) method, are an important part of the computer-aided-design process for many microwave structures and devices. However, uncertainties, inherent in the problem (e.g. temperature fluctuations) or introduced in the manufacturing processes, are difficult to capture and characterize using existing computational techniques [1], [2], [3]. Of particular interest is the analysis of fabrication tolerances, which introduce randomness in the physical dimensions and geometry [4], [1], [5, pp. 299–302]. These uncertainties ‘propagate’ through the circuit or device to introduce uncertainty in the response and system outputs. Quantifying the randomness in the circuit or device response is an essential step in the design and validation process to estimate the sensitivity of the predictions and for setting realistic design margins [2], [6].

Analyzing a single realization of the circuit, at the nominal values or otherwise, does not account for the uncertainties, which can typically only be examined by collating multiple results. The Monte Carlo method is widely used to quantify the impacts of uncertainty and randomness in numerical models and has been demonstrated to provide accurate results for electromagnetic problems [7]. However, statistics computed

via the Monte Carlo method tend to converge slowly—for example, the mean converges at a rate proportional to $\frac{1}{\sqrt{M}}$, where M is the number of trials [8, pp. 8–9]. This tends to limit the application of Monte Carlo methods for computationally large or complex problems. Other methods, such as perturbation with truncated series expansions can also be used for sensitivity and uncertainty analysis. However, perturbation is usually only valid for small changes in the input parameters [9].

Recently, methods based on generalized polynomial chaos have been proposed to more efficiently quantify large-scale uncertainty in numerical models. The polynomial chaos method is based on the orthogonal expansion of a second-order random process in the space spanned by the random input parameters [10]. The governing equations of the system are recast using a Galerkin procedure, and while the computational costs are increased, relative to the non-stochastic case, polynomial chaos techniques typically converge significantly faster than the Monte Carlo method [10]. The computational efficiency depends on the number of random inputs and the underlying complexity of the problem [10]. Furthermore, generalized polynomial chaos can provide estimates for the statistics and sensitivities from a single simulation run.

Non-intrusive methods such as stochastic collocation and pseudospectral projection using the polynomial chaos expansion and sparse-grid integration [11, pp. 78–88] have also been applied to estimate uncertainty in computational electromagnetics, for example: periodic structures [12]; passive devices [13]; compatibility and interference [14], [15]; and indoor propagation [16]. However, non-intrusive methods require multiple deterministic simulations to estimate the statistics; whereas generalized polynomial chaos using the Galerkin method typically provides more accurate and efficient solutions from a single simulation run [11, pp. 87–88].

Previous applications of generalized polynomial chaos for microwave circuits have generally not focused on full-wave simulation methods. These have examined the effects of statistical variability in the per-unit-length parameters for single- and multi-conductor transmission lines using the telegrapher’s equations and coupling from random external fields [2], [3]. FDTD-based implementations of the polynomial chaos method have largely focused on the analysis of loaded resonant cavities and free-space scattering problems [17], [18]. Generalized polynomial chaos has also been applied to examine uncertainty in other time-domain schemes, e.g. the discontinuous Galerkin method [19]. In [18] randomness in the geome-

This paper is an expanded paper from the IEEE Int. Microwave Symposium held on June 2–7, 2013 in Seattle, WA.

A.C.M. Austin and C.D. Sarris are with Edward S. Rogers Sr. Department of Electrical and Computer Engineering, University of Toronto, Toronto, ON, M5S 3G4, Canada (e-mail: acm.austin@ieec.org).

try or dimensions was modelled by an uncertainty in the material properties. While this method provides acceptable results for dielectric interfaces, highly conducting or perfect electrical conductor (PEC) boundaries result in numerical instability [17]; and is thus unsuitable for the analysis of manufacturing tolerances in typical microwave circuits.

This paper extends the novel approach outlined in [20] to overcome these limitations by modelling randomness in the geometry as an uncertainty in the FDTD computational domain. In [20] uncertainty was introduced by altering the rectilinear cell spacing of the Yee lattice; in this paper we extend the formulation to model arbitrary geometrical uncertainties using a generalized curvilinear computational mesh. The system of update equation is stable and can accurately characterize uncertain PEC geometries, making the efficient FDTD analysis of manufacturing tolerances in microwave circuits possible. A brief overview of the polynomial chaos expansion (PCE) is presented in section II; the new system of update equations is also derived by expanding the time-domain electric and magnetic fields in terms of the uncertain mesh parameters. This approach is then extended to a wider range of uncertain PEC geometries in section III. Numerical results for practical microwave circuits are presented in section IV and validated against Monte Carlo simulations.

II. MODELLING GEOMETRICAL UNCERTAINTY IN THE FDTD METHOD WITH THE PCE

Due to random manufacturing tolerances (e.g. during milling, etching or printing) individual realizations of a microwave circuit will have different, and uncertain, physical geometry and dimensions [6], [1]. These uncertainties can be expressed as random variables, characterized with appropriate probability distributions. In this analysis it is assumed the uncertainties are statistically independent; but these do not have to be identically distributed.

A. The Polynomial Chaos Expansion

Randomness in the geometry and dimensions will introduce uncertainty in the time-domain electric and magnetic fields throughout the problem space [19]. The polynomial chaos method expands these uncertain fields as a truncated summation of orthogonal basis functions, Ψ_a , in the N random variables, $\xi = \{\xi_1, \xi_2, \dots, \xi_N\}$ [10]. For example, the expansion for the uncertain E_z field component in the FDTD method can be written [19], [18]

$$E_z|_{i,j,k+\frac{1}{2}}^n(\xi) = \sum_{a=0}^P e_z^a|_{i,j,k+\frac{1}{2}}^n \Psi_a(\xi), \quad (1)$$

where $e_z^a|_{i,j,k+\frac{1}{2}}^n$ are the weighting coefficients. The number of terms is given by

$$P + 1 = \frac{(N + D)!}{N!D!}, \quad (2)$$

where D is the highest polynomial order in the expansion. The multivariate polynomial chaos basis functions can be expressed

$$\Psi_a(\xi) = \prod_{i=1}^N \phi_{m_i^a}(\xi_i), \quad (3)$$

where $\phi_{m_i^a}(\xi_i)$ is a univariate orthogonal basis in ξ_i , and m_i^a is the multi-index corresponding to the order of the expansion [11, pp. 64–67], for $a = 0 \dots P$. While any suitable orthogonal functions may be used, it can be shown that the optimal polynomial basis (providing exponential convergence), $\phi(\xi_i)$, depends on the assumed distribution of random variable ξ_i [10]. This association is termed the Wiener-Askey scheme—in which, Gaussian distributed inputs are associated with Hermite polynomials and uniformly distributed inputs with Legendre polynomials [10]. In cases where the input parameter distributions are difficult to determine (or unknown), uniform or Gaussian probability density functions (PDFs) are often assumed [11, pp. 44–46]. However, for geometrical uncertainties, the infinite limits of the Gaussian distribution are non-physical. This paper uses the approach proposed by Xiu [10], where Gaussian random variables are approximated by the Beta distribution, which has finite support; Jacobi polynomials are then used as the basis functions. The resulting multivariate basis functions are orthogonal with respect to the PDFs over Ω , with an inner product given by

$$\begin{aligned} \langle \Psi_a(\xi), \Psi_b(\xi) \rangle &= \int_{\Omega} \Psi_a(\xi) \Psi_b(\xi) w(\xi) d\xi \\ &= \langle \Psi_a^2(\xi) \rangle \delta_{a,b}. \end{aligned} \quad (4)$$

For Legendre polynomials, $w = 0.5^N$ with $\Omega \in [-1, 1]^N$; while for Jacobi polynomials, $w = \prod_{i=1}^N (1 - \xi_i)^\alpha (1 + \xi_i)^\beta$ with $\Omega \in [-1, 1]^N$; $\alpha = \beta = 3$ was used to provide an acceptable approximation [11, pp. 113–115]

B. Modelling Geometrical Uncertainties

In general, an objects' physical dimension, d , in an arbitrary planar geometry can be modelled in the FDTD method by $d = n\Delta$, where Δ is the nominal lattice dimension, and n is the number of Yee cells (subcell techniques can be used when d is not an integer multiple of Δ). Uncertainty in the length of d can be modelled by making n a random variable, keeping Δ constant [19], [18]. This process spatially distributes the uncertainty over several cells in the computational lattice around the nominal boundary. The PCE can be applied to each field component in these regions by translating the geometrical uncertainty into an uncertainty in the material properties (e.g. permittivity and conductivity) [19], [18]. However, this approach is only feasible for uncertainty in the dimensions of low-contrast dielectric materials. Highly conducting or PEC materials introduce large spurious reflections along the spatially distributed boundary, resulting in numerical instability [17, pp. 208–213].

By contrast, in this analysis, randomness in the physical dimensions and geometry are incorporated into the FDTD method by introducing uncertainty in Δ . For example, Fig. 1(a) shows a PEC corner, where uncertainties in the planar geometry—denoted by ξ_1 and ξ_2 , and indicated by the hatched regions—exist in both the \hat{x} and \hat{y} directions and extend over several Yee lattice cells. By appropriately expanding and compressing the dimensions of the mesh cells, as depicted in Fig. 1(b), randomness in the position of the

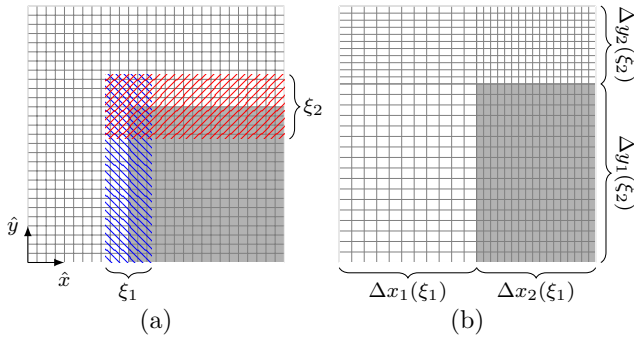


Fig. 1. Due to fabrication tolerances uncertainty is assumed to exist in the physical dimensions and geometry. For example, (a) shows the nominal lattice for a PEC corner with the hatched regions representing the uncertainty, ξ_1 and ξ_2 in the x and y directions respectively; while (b) depicts one realization formed by distorting the dimensions of the Yee lattice cells.

PEC boundaries can be realized in the FDTD computational domain. For example, the uncertainty in Δx_2 is given by

$$\Delta x_2(\xi_1) = \frac{\Delta x^{\max} + \Delta x^{\min}}{2} + \frac{\Delta x^{\max} - \Delta x^{\min}}{2} \xi_1, \quad (5)$$

where ξ_1 is a uniform or Beta distributed random variable over the interval $-1 \leq \xi_1 \leq 1$, and Δx^{\min} and Δx^{\max} represent the minimum and maximum values of the lattice spacing required to achieve the desired uncertainty. It is important to note that while the physical dimensions have changed, the ‘computational dimensions’ of the geometry have not been altered, allowing this approach to handle PEC boundaries. Equation (1) can then be applied to express each uncertain time-domain electric and magnetic field component as a function of ξ_1 and ξ_2 .

The uncertainty in the lattice spacing is distributed over a region, and similar local refinements of the cell spacing in the Yee lattice to align it with physical objects has previously been shown to be second order accurate [21, pp. 464–471]. Distorting the Yee lattice is suitable when the geometrical uncertainties can be aligned with the rectilinear mesh. While a large class of planar microwave circuits can be analyzed accordingly, this restriction is relaxed in section III, which allows for more general geometrical uncertainties by utilizing curvilinear grids.

C. Derivation of PCE-FDTD Update Equations

The expansion outlined in (1) separates the randomness in the field components from the dependence on time and position [18]. Similar expressions can be formulated for the remaining electric and magnetic field components and substituted into the FDTD update equations along with (5). The resulting expansion for the E_z field component can be

expressed as

$$\begin{aligned} \sum_{a=0}^P e_z^a |_{i,j,k+\frac{1}{2}}^{n+1} \Psi_a(\boldsymbol{\xi}) &= \frac{2\epsilon_0\epsilon_r - \sigma\Delta t}{2\epsilon_0\epsilon_r + \sigma\Delta t} \sum_{a=0}^P e_z^a |_{i,j,k+\frac{1}{2}}^n \Psi_a(\boldsymbol{\xi}) \\ &+ \frac{2\Delta t}{2\epsilon_0\epsilon_r + \sigma\Delta t} \left[\sum_{a=0}^P \frac{h_y^a |_{i+\frac{1}{2},j,k+\frac{1}{2}}^{n+\frac{1}{2}} - h_y^a |_{i-\frac{1}{2},j,k+\frac{1}{2}}^{n+\frac{1}{2}}}{\Delta x(\boldsymbol{\xi})|_i} \Psi_a(\boldsymbol{\xi}) \right. \\ &\quad \left. - \sum_{a=0}^P \frac{h_x^a |_{i,j+\frac{1}{2},k+\frac{1}{2}}^{n+\frac{1}{2}} - h_x^a |_{i,j-\frac{1}{2},k+\frac{1}{2}}^{n+\frac{1}{2}}}{\Delta y(\boldsymbol{\xi})|_j} \Psi_a(\boldsymbol{\xi}) \right]. \quad (6) \end{aligned}$$

Applying a Galerkin procedure by taking inner products with the test function $\Psi_b(\boldsymbol{\xi})$, where $b = 0, \dots, P$, and using the orthogonality condition from (4), reduces (6) to

$$\begin{aligned} e_z^b |_{i,j,k+\frac{1}{2}}^{n+1} &= \frac{2\epsilon_0\epsilon_r - \sigma\Delta t}{2\epsilon_0\epsilon_r + \sigma\Delta t} e_z^b |_{i,j,k+\frac{1}{2}}^n + \frac{2\Delta t}{2\epsilon_0\epsilon_r + \sigma\Delta t} \\ &\frac{1}{\langle \Psi_b^2 \rangle} \left[\sum_{a=0}^P \left(h_y^a |_{i+\frac{1}{2},j,k+\frac{1}{2}}^{n+\frac{1}{2}} - h_y^a |_{i-\frac{1}{2},j,k+\frac{1}{2}}^{n+\frac{1}{2}} \right) \left\langle \frac{\Psi_a(\boldsymbol{\xi})\Psi_b(\boldsymbol{\xi})}{\Delta x(\boldsymbol{\xi})|_i} \right\rangle \right. \\ &\quad \left. - \sum_{a=0}^P \left(h_x^a |_{i,j+\frac{1}{2},k+\frac{1}{2}}^{n+\frac{1}{2}} - h_x^a |_{i,j-\frac{1}{2},k+\frac{1}{2}}^{n+\frac{1}{2}} \right) \left\langle \frac{\Psi_a(\boldsymbol{\xi})\Psi_b(\boldsymbol{\xi})}{\Delta y(\boldsymbol{\xi})|_j} \right\rangle \right]. \quad (7) \end{aligned}$$

Similar update equations can be derived for the remaining E and H field components. Solving the $b = 0, \dots, P$ coupled set of update equations for the PCE coefficients yields the uncertainty in the time-domain fields throughout the lattice (1). To ensure numerical stability, the time-step is reduced to account for the smallest possible cell dimension in the distorted lattice. The convolutional implementation of the complex frequency shifted tensor perfectly matched layer (CPML) is used in this analysis to simulate propagation in unbounded media [21, pp. 294–297]. The two additional auxiliary variables for each field component in the CPML are expanded using the PCE, similar to (5)–(7).

The inner products can be precomputed using numerical integration before time-stepping commences [22]. Furthermore, for regions outside the distorted lattice, the inner products in (7) reduce to Kronecker delta functions, and thus the update equations can be decoupled and solved for $b = 0, \dots, P$ independently. The computational resources required to solve (7) are increased relative to the non-stochastic case. In general, the PCE increases memory consumption by a factor $P + 1$ and run times proportional to $(P + 1)^2$ [10], [18].

D. Estimating Response Statistics

Statistics of the fields can be readily calculated from the PCE solution; for example, the mean and variance for a E_z field component are given by [11, p. 67]

$$\mu [E_z(\boldsymbol{\xi})] = e_z^0, \quad (8)$$

$$\sigma^2 [E_z(\boldsymbol{\xi})] = \sum_{a=1}^P (e_z^a)^2 \langle \Psi_a^2 \rangle. \quad (9)$$

The PDFs can be estimated by running a Monte Carlo analysis on the PCE for the fields. The global sensitivity can be estimated using the Sobol decomposition of the polynomial chaos

expansion [23]. This yields a set of conditional variances, indicating the relative contribution each combination of input parameters makes toward the uncertainty in the response. The Sobol indices for the set of inputs u can be expressed

$$S_u = \frac{\sum_{m \in K_u} (e_z^m)^2 \langle \Psi_m^2 \rangle}{\sum_{m=1}^P (e_z^m)^2 \langle \Psi_m^2 \rangle}, \quad (10)$$

where K_u is an index to the terms in (1) that contain u [23].

Solving (7) yields the uncertainty in the time-domain fields throughout the lattice, however we are often more interested in characterizing the uncertainty in the frequency-domain S -parameters. These can be found by projecting the Fourier transform of the uncertain time-domain signals (recorded at appropriate ports) onto the basis functions. For example, $|S_{21}^b|$, for $b = 0, \dots, P$, is given by

$$|S_{21}^b(\omega)| = \left\langle \left| \frac{\sum_{a=0}^P \mathcal{F}\{v_2^a(t)\} \Psi_a(\boldsymbol{\xi})}{\sum_{a=0}^P \mathcal{F}\{v_1^a(t)\} \Psi_a(\boldsymbol{\xi})} \right|, \Psi_b(\boldsymbol{\xi}) \right\rangle \quad (11)$$

where $\mathcal{F}\{v_n^a(t)\}$ is the Fourier transform of the a^{th} coefficient in the uncertain time-domain signal recorded at port n . Equation (11) can be solved using numerical cubature, and the statistics and sensitivity for the S -parameters can be found by applying (8)–(10).

III. LOCAL MESH DISTORTION

The method outlined in the previous section—namely, globally distorting the cell spacing of the rectilinear Yee mesh—cannot be used when the uncertainties in the physical geometry are aligned but statistically independent. For example, Fig. 2 shows a microstrip filter where uncertainties in the (nominally equal, and thus geometrically aligned) stub lengths $L_{1..3}$ are statistically independent. In this and similar such cases, randomness in the physical geometry can be incorporated into the FDTD method by introducing uncertainty in the local computational mesh. To accomplish this, a curvilinear FDTD mesh is defined around each uncertain portion of the geometry and parameterized in terms of the random variables. Fig. 2 shows how three local curvilinear computational meshes can be distorted to achieve the desired (independent) uncertainties in $L_{1..3}$. A brief derivation for the curvilinear FDTD update equations expanded using generalized polynomial chaos follows—for the general case, where the curvilinear mesh is parameterized by N random variables, $\boldsymbol{\xi} = \{\xi_1, \dots, \xi_N\}$.

A. Application of Polynomial Chaos to Curvilinear FDTD

Uncertainty in the curvilinear computational mesh will introduce uncertainty in the time-domain co- and contravariant electric and magnetic field components. The polynomial chaos expansion can then be applied to each field component, for example, the uncertain contravariant E^1 fields can be expanded in terms of $\boldsymbol{\xi}$,

$$E^1(i, j, k, n, \boldsymbol{\xi}) = \sum_{a=0}^P a e^1|_{i,j,k}^n \Psi_a(\boldsymbol{\xi}) \quad (12)$$

where $a e^1$ are the expansion coefficients, and $\Psi(\boldsymbol{\xi})$ is given by (3). Similar expressions can be derived for the remaining

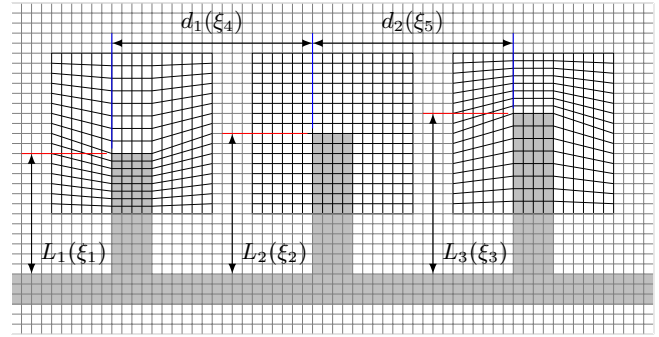


Fig. 2. The length of each nominally equal stub, $L_{1..3}$, depends on the independent random variables, $\xi_{1..3}$, which are characterized by appropriate PDFs. The local curvilinear mesh surrounding each stub is parameterized in terms of $\xi_{1..3}$. The polynomial chaos method is then used to expand the time-domain electric and magnetic fields in terms of the curvilinear mesh-distortion parameters. Uncertainty in $d_{1..2}$ can be incorporated using the approach outlined in section II.

co- and contravariant electric and magnetic field components. Equation (12) can be substituted into the curvilinear FDTD update equation for the E^1 component [24], resulting in

$$\begin{aligned} \sum_{a=0}^P a e^1|_{i,j,k}^{n+1} \Psi_a(\boldsymbol{\xi}) &= \sum_{a=0}^P \alpha(\boldsymbol{\xi})|_{i,j,k} a e^1|_{i,j,k}^n \Psi_a(\boldsymbol{\xi}) \\ &+ \frac{\beta(\boldsymbol{\xi})|_{i,j,k}}{V(\boldsymbol{\xi})|_{i,j,k}^{E^1}} \left[\sum_{a=0}^P \left(a h_3|_{i,j,k}^{n+\frac{1}{2}} - a h_3|_{i,j-1,k}^{n+\frac{1}{2}} \right) \Psi_a(\boldsymbol{\xi}) \right. \\ &\quad \left. - \sum_{a=0}^P \left(a h_2|_{i,j,k}^{n+\frac{1}{2}} - a h_2|_{i,j,k-1}^{n+\frac{1}{2}} \right) \Psi_a(\boldsymbol{\xi}) \right] \quad (13) \end{aligned}$$

In (13) $V(\boldsymbol{\xi})|_{i,j,k}^{E^1}$ is the volume of the $\{i, j, k\}$ cell in the uncertain curvilinear FDTD mesh (defined for contravariant E^1 field), and

$$\alpha(\boldsymbol{\xi})|_{i,j,k} = \frac{2\epsilon_0\epsilon_r(\boldsymbol{\xi})|_{i,j,k} - \sigma(\boldsymbol{\xi})|_{i,j,k}\Delta t}{2\epsilon_0\epsilon_r(\boldsymbol{\xi})|_{i,j,k} + \sigma(\boldsymbol{\xi})|_{i,j,k}\Delta t},$$

and

$$\beta(\boldsymbol{\xi})|_{i,j,k} = \frac{2\Delta t}{2\epsilon_0\epsilon_r(\boldsymbol{\xi})|_{i,j,k} + \sigma(\boldsymbol{\xi})|_{i,j,k}\Delta t}$$

are the coefficients due to uncertainty in the material properties [18]. A Galerkin procedure is applied for $b = 0, \dots, P$, reducing (13) to

$$\begin{aligned} b e^1|_{i,j,k}^{n+1} &= \frac{1}{\langle \Psi_b^2 \rangle} \sum_{a=0}^P b e^1|_{i,j,k}^n \left\langle \alpha(\boldsymbol{\xi})|_{i,j,k} \Psi_a(\boldsymbol{\xi}) \Psi_b(\boldsymbol{\xi}) \right\rangle \\ &+ \left(a h_3|_{i,j,k}^{n+\frac{1}{2}} - a h_3|_{i,j-1,k}^{n+\frac{1}{2}} - a h_2|_{i,j,k}^{n+\frac{1}{2}} + a h_2|_{i,j,k-1}^{n+\frac{1}{2}} \right) \\ &\quad \cdot \left\langle \frac{\beta(\boldsymbol{\xi})|_{i,j,k}}{V(\boldsymbol{\xi})|_{i,j,k}^{E^1}} \Psi_a(\boldsymbol{\xi}) \Psi_b(\boldsymbol{\xi}) \right\rangle. \quad (14) \end{aligned}$$

Similar expressions can be derived for the remaining contravariant electric and magnetic field components. The covariant field components are computed by projecting the contravariant field components onto the curvilinear mesh. Spatial averaging is required as the components are not collocated.

The update expression for the coefficients of the uncertain covariant ${}_b e_1$ field is thus given by

$$\begin{aligned}
 {}_b e_1|_{i,j,k}^{n+1} &= \frac{1}{\langle \Psi_b^E \rangle} \sum_{a=0}^P a e^1|_{i,j,k}^{n+1} \left\langle g_{11}^E(\xi) \Big|_{i,j,k} \Psi_a(\xi) \Psi_b(\xi) \right\rangle \\
 &+ \left[a e^2|_{i,j,k}^{n+1} + a e^2|_{i,j-1,k}^{n+1} + a e^2|_{i+1,j,k}^{n+1} + a e^2|_{i+1,j-1,k}^{n+1} \right] \\
 &\cdot \left\langle \frac{g_{12}^E(\xi)}{4} \Big|_{i,j,k} \Psi_a(\xi) \Psi_b(\xi) \right\rangle + \left[a e^3|_{i,j,k}^{n+1} + a e^3|_{i+1,j,k}^{n+1} \right. \\
 &\left. + a e^3|_{i+1,j,k-1}^{n+1} + a e^3|_{i,j,k-1}^{n+1} \right] \left\langle \frac{g_{13}^E(\xi)}{4} \Big|_{i,j,k} \Psi_a(\xi) \Psi_b(\xi) \right\rangle
 \end{aligned} \quad (15)$$

where $g_{11}^E(\xi)$, $g_{12}^E(\xi)$ and $g_{13}^E(\xi)$ are the projection vectors for the curvilinear E -mesh in the presence of uncertainty. The computation of these quantities is briefly outlined in Appendix A. Similar to the analysis in section II, the inner products in (14) and (15) are precomputed, however, unlike (7) these must be stored for each cell in the curvilinear mesh. The storage requirements for the inner products grow proportional to $(P+1)^2$, but in practice these can be substantially reduced by using a hash table. Outside the curvilinear mesh, there is no uncertainty in the volume or projection vectors, and thus the inner products in (14) and (15) reduce to Kronecker delta functions, and the $b = 0, \dots, P$ update equations are decoupled.

B. Numerical Stability

The stability condition of a general non-orthogonal explicit FDTD update scheme is given by [21, pp. 485–486]

$$\Delta t \leq \frac{1}{c \sup \left(\sqrt{\sum_{l=1}^3 \sum_{m=1}^3 g^{l,m}} \right)}, \quad (16)$$

where \sup denotes the maximum value throughout the curvilinear mesh, c is the velocity of propagation and $g^{l,m}$ is the inverse metric [21, pp. 481–482]. The update equation for each coefficient in the PCE-FDTD scheme (14) can be considered a weighted summation of $P+1$ non-stochastic curvilinear FDTD update equations over the range of mesh distortions and lattice cell dimensions. Thus the stable time step for (14) can be set using (16), given the maximum uncertainty in the computational mesh. No late time instabilities were observed in any of the examples considered, or in test cases run for 1×10^5 time steps. All Monte-Carlo simulations were also run using the same time step to ensure fair comparisons.

IV. NUMERICAL RESULTS

A. Low Pass Microstrip Filter

Fig. 3 shows a microstrip implementation of a 5.6 GHz low pass filter, with three uncertain dimensions identified, $\{d_1, d_2, d_3\}$. The FDTD computational lattice is $130 \times 100 \times 36$ cells in size (including the CPML), and the nominal cell dimensions are: $\Delta x = 0.4064$ mm; $\Delta y = 0.4233$ mm and $\Delta z = 0.265$ mm [25]. The filter is excited at port 1 using a modulated Gaussian pulse with a 10 GHz centre frequency and solved to 4000 time steps. The Monte Carlo method is

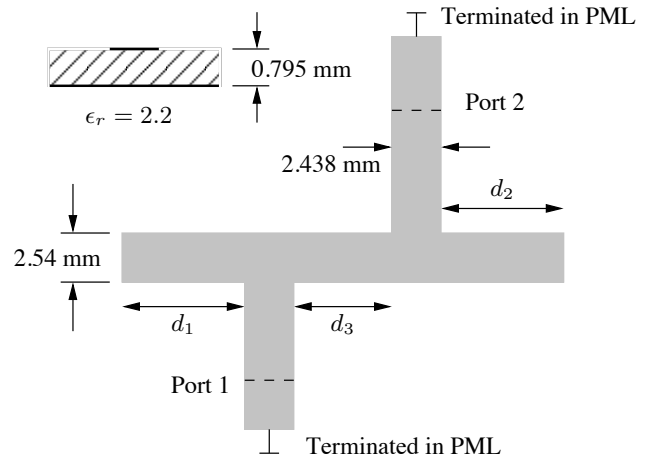


Fig. 3. Microstrip implementation of a low pass filter with uncertain dimensions: $d_1 = 5.69 \pm 0.5$ mm; $d_2 = 5.69 \pm 0.5$ mm; and $d_3 = 4.064 \pm 1.0$ mm. Other dimensions are assumed to remain constant.

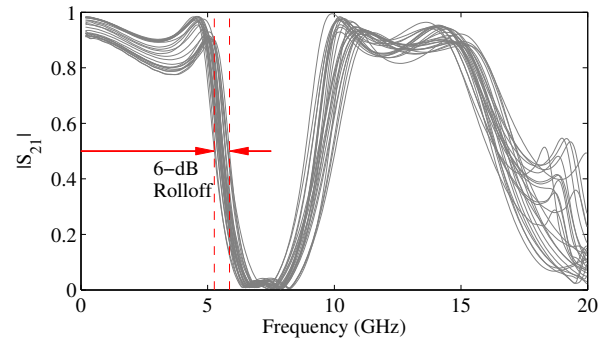
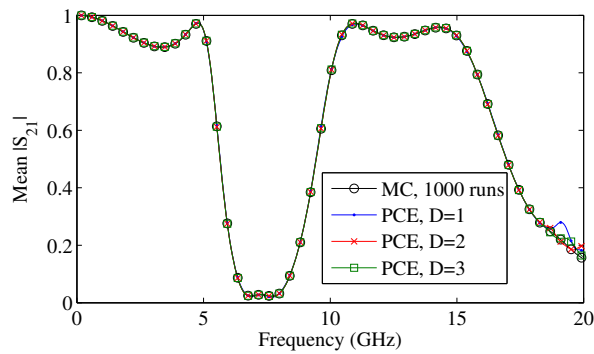


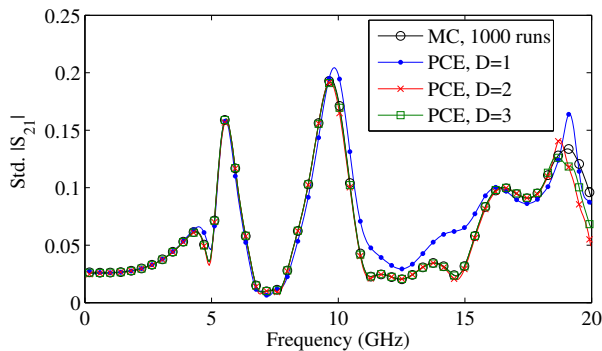
Fig. 4. Magnitude of filter S_{21} for 25 samples drawn from the Monte Carlo simulations. Each grey line represents one FDTD simulation with a particular set of input parameters (stub lengths). The 6-dB roll-off frequency is observed to vary with the stub lengths.

applied by generating a set of 1000 uniformly distributed random dimensions, appropriately scaling the lattice spacing, and solving each realization of the circuit independently. Fig. 4 shows the magnitude of the filter S_{21} for 25 realizations of the random stub lengths over a 0–20 GHz frequency range. Changes to the stub lengths alters the frequency-domain response of the filter, including the magnitude of the ripple in the pass- and stop-bands and the roll-off. Fig. 5(a) shows the mean S_{21} magnitude computed using Monte Carlo simulations and the FDTD-PCE formulation outlined in section II-C. The corresponding standard deviation about the mean values is shown in Fig. 5(b). The standard deviation is observed to increase in the roll-off regions of the filter response, indicating an increased degree of uncertainty exists in the results at these points.

The polynomial chaos expansion is truncated at order $D = \{1, 2, 3\}$, and the time-domain e_z^m field terms (recorded at ports 1 and 2) are projected into the frequency-domain via (11) to determine the uncertainty in the S -parameter statistics. As shown in Fig. 5(a), the mean is well predicted across the entire frequency range, and the convergence against the



(a)

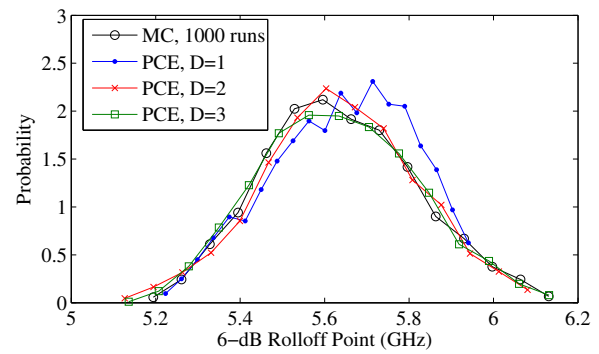


(b)

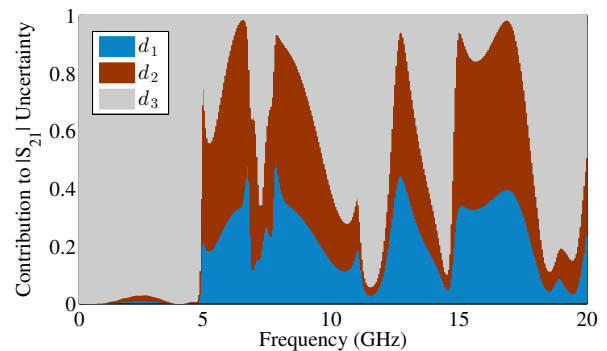
Fig. 5. Comparison of the (a) Mean and (b) Standard deviation in $|S_{21}|$ computed using 1000 Monte Carlo (MC) trials and via polynomial chaos expansions (PCE).

Monte Carlo results improves with increasing D . However, small deviations in the prediction of the mean occur beyond 18 GHz. Similar effects are observed in the prediction of the standard deviation beyond 10 GHz. The differences between the polynomial chaos results and Monte Carlo simulations arise from two effects. Firstly, higher statistical moments, such as the standard deviation and kurtosis, generally require higher order polynomial terms to converge to the same level of error in the mean prediction [10]. Secondly, at higher frequencies the change in the electrical lengths of the stubs is larger, causing increased uncertainty, which requires higher order polynomial terms to converge—this effect is also observed in the subset of Monte Carlo simulations shown in Fig. 4.

Fig. 6(a) shows PDFs of the 6 dB filter roll-off frequency estimated from 1000 Monte Carlo trials and via the polynomial chaos expansions. Accurate models for the expected spread are important to assess the sensitivity of the predictions, and can provide a measure of confidence in simulated results. The shape of the PDF converges as the order of expansion increases and generally compares well with the Monte Carlo results. While 1000 Monte Carlo trials are sufficient to capture the statistics around the mean, further trials would be required to improve accuracy in the tails of the distribution. Fig. 6(b) shows the relative contribution of each stub length to the uncertainty in $|S_{21}|$ computed via (10). The uncertainty in the pass band ripple is dominated by d_3 , the stub separation; whereas in the transition regions and the stop band, the lengths



(a)



(b)

Fig. 6. (a) Probability density functions of the low pass filter 6 dB roll-off point computed using 1000 Monte Carlo trials and via polynomial chaos expansions. (b) Relative contribution of each stub length to the uncertainty in $|S_{21}|$ computed using the $D = 3$ expansion.

of the stubs have greater impact. This analysis is valuable as it indicates which parameters should be targeted to have the greatest reduction in the variability of the response.

The simulation time for each Monte Carlo trial is approximately 4 minutes (on a 3.3 GHz Intel i3 processor); 1000 trials thus take 2.5 days. By comparison, the polynomial chaos method requires approximately 8, 23 and 58 minutes for $D = 1-3$ respectively. The additional overhead in computing the inner products and post processing the results is small compared the FDTD run-times.

B. Cascaded Stub Line Filter

The curvilinear PCE-FDTD method is applied to estimate the response statistics for the lowpass cascaded stub line filter shown in Fig. 2. Two and four stub designs are considered for a 6 GHz operating frequency. Due to fabrication tolerances, uncertainty exists in the stub lengths, L , and separation, d . The nominal dimensions are $d = 15$ mm and $L = 12.5$ mm, and the uncertainties are assumed to be Beta distributed with standard deviation, $\sigma = 0.167$ mm and limits ± 0.5 mm. The rectilinear parent mesh is $85 \times 65 \times 30$ cells in size (and terminated in a 10 cell thick CPML), while the curvilinear sub-meshes are $26 \times 26 \times 26$ and defined around the stubs. Covariant components on the boundaries on the curvilinear mesh are aligned with appropriate field components in the rectilinear lattice and are exchanged at each time step. The

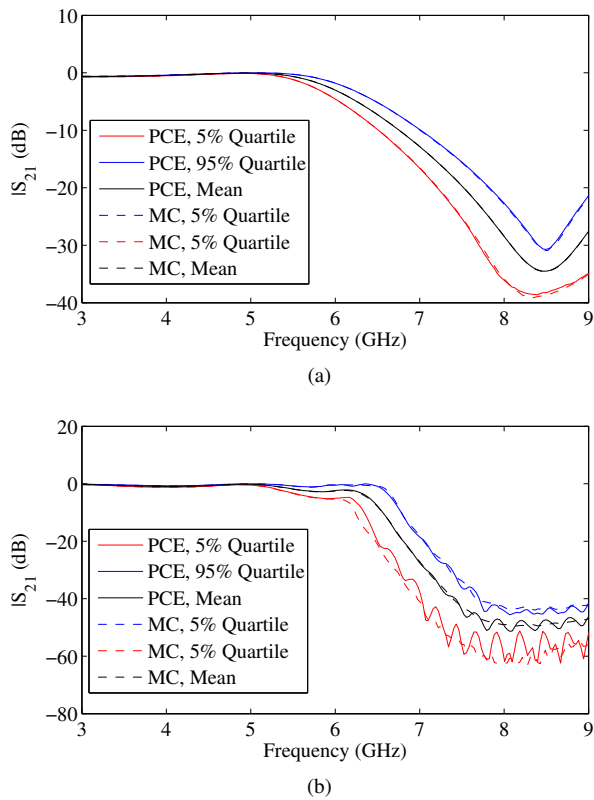


Fig. 7. Mean and 90% confidence intervals of $|S_{21}|$ in dB units for the cascaded stub line filter computed using the PCE truncated at $D = 3$, and 1000 Monte Carlo (MC) trials. (a) Two-stub filter with Beta distributed uncertainties, $\sigma = 0.167$ mm in L_1 , L_2 and d_1 ; and (b) four-stub filter with $\sigma = 0.167$ mm in L_1 – L_4 .

nominal cell is 0.25 mm^3 , and the smallest cell dimensions in the rectilinear mesh distortion region are used to set the stable time-step; in this case $\Delta t = 0.238$ ps.

Fig. 7(a) shows estimates of the mean $|S_{21}|$ and 90% confidence intervals for the two-stub filter computed via the PCE truncated at $D = 3$ and 1000 Monte Carlo trials; the close agreement over 3–9 GHz demonstrates the validity of the polynomial chaos approach. The limits of the 90% confidence interval are found from the PDFs, such that 5% of the data are expected to fall outside upper and lower bounds respectively. In the passband there is little deviation from the mean $|S_{21}|$, indicating the design is relatively insensitive to the fabrication uncertainty. However, in the transition region and stopband the 90% confidence interval is observed to increase with frequency. Random displacement of the open circuited stubs alters the input impedance, shifting the resonant frequency of the structure and thereby introducing uncertainty in the filter roll-off characteristics.

Sharper roll-off can be achieved by using additional stubs—e.g. Fig. 7(b) shows $|S_{21}|$ for a four stub structure with greater attenuation at the expense of increased ripple in the passband. However, relative to the two stub case, the uncertainty in the filter characteristics is observed to increase. The filter elements are cascaded and thus uncertainty introduced at each stage will accumulate. A greater deviation between the statistics computed with the PCE and Monte Carlo simulations is also

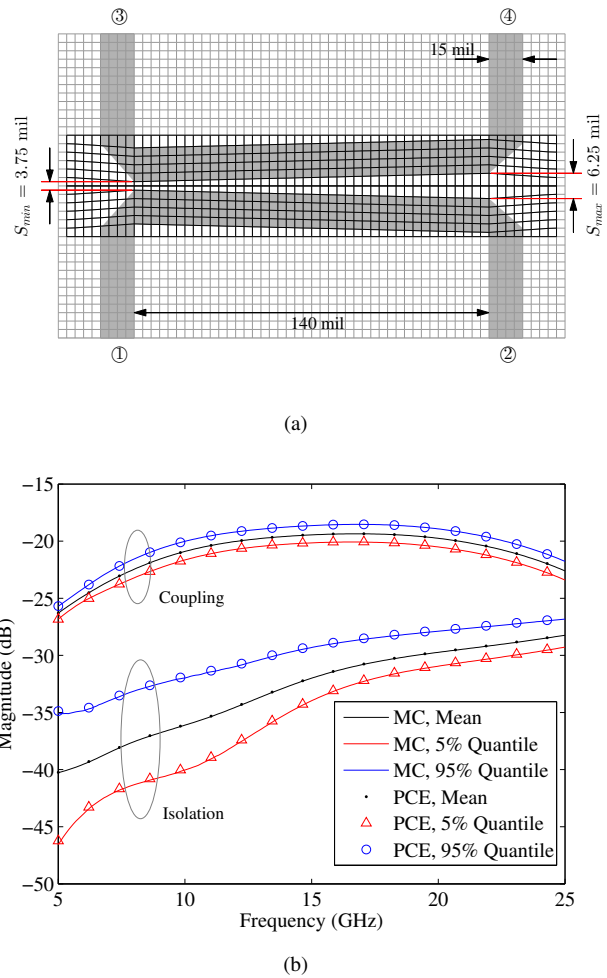


Fig. 8. (a) Curvilinear FDTD mesh for a microstrip implementation of a 20 dB 10–20 GHz directional coupler with uncertain separation between the coupled lines (dimensions are not drawn to scale); (b) Mean and 95% confidence intervals for the coupling, $|S_{13}|$, and isolation, $|S_{14}|$, computed using 1000 Monte Carlo trials and the curvilinear PCE-FDTD truncated at $D = 4$.

observed. The PCE can be interpreted as an interpolation in the random space spanned by the input parameters. Depending on the complexity of the interactions between the filter elements higher order terms may be required to achieve convergence. Nonetheless, the results shown in Fig. 7(b) provide a good approximation to the actual statistics, given the reduction in computational costs (approximately 12 hours for the single PCE simulation; and 150 hours for 1000 Monte Carlo trials).

C. Directional Coupler

Fig. 8(a) shows a microstrip implementation of a 20 dB directional coupler designed to operate over 10–20 GHz [26, pp. 390–392]. The thickness of the $\epsilon_r = 2.2$ substrate is 5 mil (1 mil = $25.4 \mu\text{m}$) and the corners of the lines are mitted to minimize reflections. Due to fabrication tolerances, uncertainty exists in the orientation and separation of the coupled lines. The random deviation of each line from the nominal (parallel) configuration is statistically independent and assumed to be uniformly distributed between 3.75–6.25 mil, with a nominal separation of 5 mil. The other dimensions

are assumed to remain constant. Similar to the cascaded stub filter described in section IV-B, a curvilinear FDTD mesh is defined around each coupled line and parameterized in terms of the random deviations. The circuit is excited with a 15 GHz modulated Gaussian pulse at port 1 (the remaining ports are terminated in the PML), and the uncertainty in the response is estimated using the curvilinear PCE-FDTD method outlined in section III.

Input signals from port 1 are coupled into port 3, while being isolated from port 4. Fig. 8(b) show statistics for the coupling, $|S_{13}|$, and isolation, $|S_{14}|$ estimated from 1000 Monte Carlo trials and the curvilinear PCE-FDTD truncated at order $D = 4$; good agreement is found across the 5–25 GHz frequency range. Randomness in the relative separation and orientation of the coupled lines alters their even and odd mode capacitance and characteristic impedance and thereby introduces uncertainty in the coupling and isolation. For example, at 15 GHz the 95% of the data is expected to fall between -18.5 dB and -20.2 dB. By contrast, the relative uncertainty in the isolation is considerably larger, particularly at lower frequencies. The time required to simulate this circuit with the fields expanded to $D = 4$ is 4.5 hours, while 1000 Monte Carlo trials take approximately 7 days.

V. CONCLUSIONS

Randomness in the physical dimensions of microwave circuits—for example, fabrication tolerances introduced during the milling or etching process—induces randomness and uncertainty in their response. Characterizing the sensitivities and uncertainties using numerical simulation tools is advantageous, but often requires excessive computational resources, e.g. Monte Carlo sampling. This paper develops novel FDTD-based algorithms to model uncertainties in the physical geometry and dimensions by expanding the time-domain fields using orthogonal polynomial chaos basis functions. The geometrical uncertainties are parameterized and incorporated into the FDTD method by appropriately distorting the rectilinear or curvilinear computational mesh. The resulting coupled system of update equations is solved to estimate the statistics and sensitivities of the time-domain fields (and S -parameters) from a single simulation run. The methods are validated by examining uncertainty in the dimensions of two microstrip filters. The statistics of the solutions agree closely with Monte Carlo results over the range of operating frequencies and are achieved at significantly lower computational cost.

APPENDIX A CURVILINEAR MESH WITH UNCERTAINTY

Fig. 9 shows the E -field unit cell for a three-dimensional curvilinear FDTD lattice; the dual H -field mesh is defined by connecting the circumcentres of the E cells. The unitary vectors are given by \mathbf{A}_1 , \mathbf{A}_2 and \mathbf{A}_3 , which are aligned with the co-variant E fields. The g -metrics used in (15) are given by

$$g_{n,m}^E|_{i,j,k} = \mathbf{A}_n^E|_{i,j,k} \cdot \mathbf{A}_m^E|_{i,j,k}. \quad (17)$$

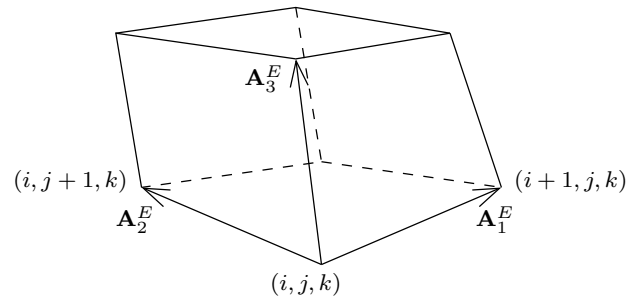


Fig. 9. Unit cell for the curvilinear E mesh, with the unitary vectors identified. The connectivity mesh remains rectilinear, and cells are appropriately distorted to account for the geometrical uncertainties.

While the volume associated with the contravariant E^1 field component is given by [27, pp. 52–53]

$$V|_{i,j,k}^{E^1} = 0.25 \mathbf{A}_1^E|_{i,j,k} \cdot \left[\left(\mathbf{A}_2^H|_{i+1,j,k} + \mathbf{A}_2^H|_{i+1,j,k+1} \right) \times \left(\mathbf{A}_3^H|_{i+1,j,k} + \mathbf{A}_3^H|_{i+1,j+1,k} \right) \right], \quad (18)$$

where A^E and A^H are the unitary vectors for the E and H lattices respectively. Similar expressions can be derived for the volumes of the remaining E and H field components. The FDTD update equations for the co- and contravariant components (in the absence of uncertainty) can be derived from the expansion of the field in terms of the unitary and reciprocal mesh vectors [21, pp. 480–486].

Uncertainty in the g -metrics and volumes is introduced by appropriately distorting the lattice coordinates to align the mesh with particular realizations of the random dimensions and geometry. It should be noted that the inner products in (13)–(15) are computed using numerical quadrature, therefore, it is not necessary to obtain closed form expressions for (17) or (18) in terms of the distortions.

REFERENCES

- [1] L. R. A. X. de Menezes, A. O. Paredes, H. Abdalla, and G. A. Borges, “Modeling device manufacturing uncertainty in electromagnetic simulations,” in *Digest IEEE MTT-S Int. Microw. Symp.*, 2008, pp. 1385–1388.
- [2] P. Manfredi and F. G. Canavero, “Polynomial chaos-based tolerance analysis of microwave planar guiding structures,” in *Digest IEEE MTT-S Int. Microw. Symp.*, 2011, pp. 1132–1136.
- [3] —, “Polynomial chaos for random field coupling to transmission lines,” *IEEE Trans. Electromagn. Comput.*, vol. 54, no. 3, pp. 677–680, June 2012.
- [4] M. Nhat Pham, J. Müller, and A. F. Jacob, “Measurement and fabrication uncertainties in high-directivity microstrip couplers,” in *Proc. European Microw. Conf.*, 2012, pp. 479–482.
- [5] R. Garg, P. Bhartia, I. Bahl, and A. Ittipiboon, *Microstrip Antenna Design Handbook*. Boston: Artech House, 2001.
- [6] R. V. Snyder, “Practical aspects of microwave filter development,” *IEEE Microw. Mag.*, vol. 8, no. 2, pp. 42–54, April 2007.
- [7] F. Hastings, J. Schneider, and S. Broschat, “A Monte-Carlo FDTD technique for rough surface scattering,” *IEEE Trans. Antennas Propag.*, vol. 43, no. 11, pp. 1183–1191, 1995.
- [8] O. P. Le Maître and O. M. Knio, *Spectral Methods for Uncertainty Quantification With Applications to Computational Fluid Dynamics*. Heidelberg: Springer-Verlag, 2010.
- [9] M. S. Gilbert and F. L. Teixeira, “A small-perturbation automatic-differentiation method for determining uncertainty in computational electromagnetics,” *IEEE Trans. Antennas Propag.*, vol. 60, no. 11, pp. 5305–5314, Nov. 2012.

- [10] D. Xiu and G. Karniadakis, "The Wiener-Askey polynomial chaos for stochastic differential equations," *SIAM J. Sci. Comput.*, vol. 24, no. 2, pp. 619–644, 2002.
- [11] D. Xiu, *Numerical Methods for Stochastic Computations: A Spectral Method Approach*. Princeton, NJ: Princeton University Press, 2010.
- [12] J. S. Ochoa and A. C. Cangellaris, "Expedient electromagnetic analysis of the impact of statistical disorder in periodic waveguides," *IEEE Trans. Microw. Theory Tech.*, vol. 60, no. 12, pp. 3919–3926, Dec. 2012.
- [13] P. Sumant, H. Wu, A. Cangellaris, and N. Aluru, "Reduced-order models of finite element approximations of electromagnetic devices exhibiting statistical variability," *IEEE Trans. Antennas Propag.*, vol. 60, no. 1, pp. 301–309, Jan. 2012.
- [14] H. Bağcı, A. C. Yucel, J. S. Hesthaven, and E. Michielssen, "A fast Stroud-based collocation method for statistically characterizing EMI/EMC phenomena on complex platforms," *IEEE Trans. Electromagn. Compat.*, vol. 51, no. 2, pp. 301–311, 2009.
- [15] A. C. Yucel, H. Bağcı, and E. Michielssen, "An adaptive multi-element probabilistic collocation method for statistical EMC/EMI characterization," *IEEE Trans. Electromagn. Compat.*, 2013.
- [16] A. C. M. Austin, N. Sood, J. Siu, and C. D. Sarris, "Application of polynomial chaos to quantify uncertainty in deterministic channel models," *IEEE Trans. Antennas Propag.* (accepted for publication), 2013.
- [17] R. S. Edwards, "Uncertainty analyses in computational electromagnetism," Ph.D. dissertation, The University of York, York, UK, March 2009.
- [18] R. S. Edwards, A. C. Marvin, and S. J. Porter, "Uncertainty analyses in the finite-difference time-domain method," *IEEE Trans. Electromagn. Compat.*, vol. 52, no. 1, pp. 155–163, Feb. 2010.
- [19] C. Chauvière, J. S. Hesthaven, and L. Lurati, "Computational modeling of uncertainty in time-domain electromagnetics," *SIAM J. Sci. Comput.*, vol. 28, no. 2, pp. 751–775, 2006.
- [20] A. C. M. Austin and C. D. Sarris, "Efficient analysis of parameter uncertainty in FDTD models of microwave circuits using polynomial chaos," in *Digest IEEE MTT-S Int. Microw. Symp.*, 2013.
- [21] A. Taflov and S. C. Hagness, *Computational Electrodynamics: The Finite-Difference Time-Domain Method*, 3rd ed. Boston: Artech House, 2005.
- [22] R. Cools and A. Haegemans, "Algorithm 824: CUBPACK: A package for automatic cubature; framework description," *ACM. Trans. Math. Software*, vol. 29, no. 3, pp. 287–296, Sept. 2003.
- [23] T. Crestaux, O. Le Maitre, and J.-M. Martinez, "Polynomial chaos expansion for sensitivity analysis," *Reliab. Eng. Syst. Safe.*, vol. 94, no. 7, pp. 1161–1172, 2009.
- [24] S. D. Gedney and J. A. Roden, "Numerical stability of nonorthogonal FDTD methods," *IEEE Trans. Antennas Propag.*, vol. 48, no. 2, pp. 231–239, Feb. 2000.
- [25] D. Sheen, S. Ali, M. Abouzahra, and J. Kong, "Application of the three-dimensional finite-difference time-domain method to the analysis of planar microstrip circuits," *IEEE Trans. Microw. Theory Tech.*, vol. 38, no. 7, pp. 849–857, 1990.
- [26] N. Kinayman and M. I. Aksun, *Modern Microwave Circuits*. Norwood, MA: Artech House, 2005.
- [27] J. A. Roden, "Broadband electromagnetic analysis of complex structures with the finite-difference time-domain technique in general curvilinear coordinates," Ph.D. dissertation, University of Kentucky, Lexington, Kentucky, 1997.



Costas D. Sarris received the Ph.D. degree in electrical engineering and M.Sc. degree in applied mathematics from the University of Michigan, Ann Arbor, in 2002.

He is currently a Full Professor and the Eugene V. Polistuk Chair in Electromagnetic Design at the Department of Electrical and Computer Engineering and an Associate Chair of the Division of Engineering Science, University of Toronto, Toronto, ON, Canada. His research interests are in the area of numerical electromagnetics, with emphasis on high-order, multiscale/multi-physics computational methods, modeling under stochastic uncertainty, as well as applications of numerical methods to wireless channel modeling, wave-propagation in complex media and metamaterials, biomedical imaging and hyperthermia, wireless power transfer and electromagnetic compatibility/interference (EMI/EMC) problems.

Prof. Sarris was the recipient of the IEEE MTT-S Outstanding Young Engineer Award in 2013 and an Early Researcher Award from the Ontario Government in 2007. His students have received paper awards at the 2009 IEEE MTT-S International Microwave Symposium, the 2008 Applied Computational Electromagnetics Society Conference, and the 2008 and 2009 IEEE International Symposia on Antennas and Propagation. He currently serves as an associate editor for the IEEE TRANSACTIONS ON MICROWAVE THEORY AND TECHNIQUES. He was the Technical Program Committee Vice-Chair for the 2012 IEEE MTT-S International Microwave Symposium, an Area Editor (Numerical Modeling) for the IEEE Microwave Magazine and an Associate Editor for the IEEE MICROWAVE AND WIRELESS COMPONENTS LETTERS.



Andrew C. M. Austin received the B.E. (Hons.) and Ph.D. degrees in electrical and electronic engineering from the University of Auckland, Auckland, New Zealand, in 2007 and 2012, respectively.

He is currently a Postdoctoral Fellow in the Edward S. Rogers Sr. Department of Electrical and Computer Engineering at the University of Toronto, Toronto, ON, Canada. His research interests include radiowave propagation modelling, computational electromagnetics and uncertainty analysis.

Dr. Austin was awarded a New Zealand Tertiary Education Commission Bright Futures Top Achiever Doctoral Scholarship from 2007–2011.